Solar Phys (2012) 279:207–229
DOI 10.1007/s11207-012-9969-9

Validation of the 3D AMR SIP–CESE Solar Wind Model for Four Carrington Rotations

Xueshang Feng · Liping Yang · Changqing Xiang · Caowei Jiang · Xiaopeng Ma · S.T. Wu · DingKun Zhong · Yufen Zhou

Received: 1 June 2011 / Accepted: 10 March 2012 / Published online: 6 April 2012

Abstract We carry out the adaptive mesh refinement (AMR) implementation of our solar–interplanetary space-time conservation element and solution element (CESE) magnetohydrodynamic model (SIP–CESE MHD model) using a six-component grid system (Feng, Zhou, and Wu, *Astrophys. J.* **655**, 1110, 2007; Feng *et al.*, *Astrophys. J.* **723**, 300, 2010). By transforming the governing MHD equations from the physical space (x, y, z) to the computational space (ξ, η, ζ) while retaining the form of conservation (Jiang *et al.*, *Solar Phys.* **267**, 463, 2010), the SIP–AMR–CESE MHD model is implemented in the reference coordinates with the aid of the parallel AMR package PARAMESH available at http://sourceforge.net/projects/paramesh/. Meanwhile, the volumetric heating source terms derived from the topology of the magnetic-field expansion factor and the minimum angular separation (at the photosphere) between an open-field foot point and its nearest coronal-hole boundary are also included. We show the preliminary results of applying the SIP–AMR–CESE MHD model for simulating the solar-wind background of different solar-activity phases by comparison with SOHO observations and other spacecraft data from OMNI. Our numerical results show overall good agreements in the solar corona and in interplanetary space with these multiple-spacecraft observations.

Keywords Solar wind · Magnetohydrodynamics (MHD) · Numerical simulation

X. Feng (✉) · L. Yang · C. Xiang · C. Jiang · X. Ma · D.K. Zhong · Y. Zhou
SIGMA Weather Group, State Key Laboratory for Space Weather, Center for Space Science and Applied Research, Chinese Academy of Sciences, Beijing 100190, China
e-mail: fengx@spaceweather.ac.cn

L. Yang · C. Jiang · X. Ma
College of Earth Sciences, Graduate University of Chinese Academy of Sciences, Beijing 100049, China

S.T. Wu
Center for Space Plasma and Aeronomic Research, The University of Alabama in Huntsville, Huntsville, AL 35899, USA

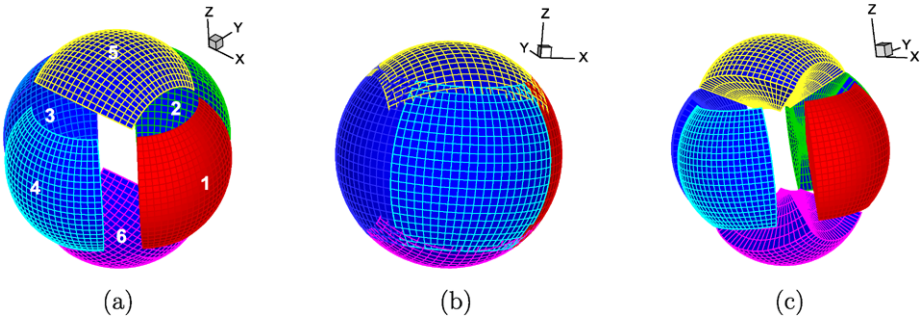

Figure 1 Six-component grid: (a) a spherical overset grid consisting of six identical components; (b) dividing a sphere into six identical components with partial overlap; (c) stacking the spherical meshes of each component up in the radial direction.

1. Introduction

In quantitatively modeling the solar-wind structures, 3D global MHD models have been developed (*e.g.* Mikić *et al.*, 1999; Lionello, Linker, and Mikić, 2009; Riley *et al.*, 2006; Roussev *et al.*, 2003; Tóth *et al.*, 2005; Cohen *et al.*, 2008; Lugaz *et al.*, 2011; Tóth *et al.*, 2012; Usmanov and Goldstein, 2006; Feng, Zhou, and Wu, 2007; Nakamizo *et al.*, 2009; van der Holst *et al.*, 2010; Feng *et al.*, 2010). As pointed out by space-weather scientists (*e.g.* Dryer, 2007; Aschwanden *et al.*, 2008; Watermann *et al.*, 2009; Feng, Xiang, and Zhong, 2011), high-performance computational models require further improvements in order to make real- or faster than real-time numerical predictions of adverse space-weather events and their influence on the geospace environment. On one hand, numerical solutions to the governing magnetohydrodynamic (MHD) equations currently used for the numerical space-weather modeling from the Sun to Earth or beyond are typically feasible only on massively parallel computers. On the other hand, one numerical challenge is due to the presence of different temporal and spatial scales on which solar-wind plasma occurs throughout the vast solar–interplanetary space of these problems. Therefore, high-performance parallel computational methods capable of better resolving the solution features of these flows are required. The objective of the present article is to consider the scalable, massively parallel, block-based, adaptive-mesh refinement (AMR) implementation on a six-component grid system (Figure 1) for our three-dimensional (3D) SIP–CESE MHD model (Feng, Zhou, and Wu, 2007; Feng *et al.*, 2010).

In order to solve numerical problems with multi-orders of spatial/temporal scales and minimize memory requirements and CPU time, the AMR technique has become a mature tool to refine or coarsen mesh grids with the expected spatial resolution according to spatial gradients of physical quantities. To support parallel implementation in numerically solving partial differential equations (PDEs), a number of AMR software infrastructure packages have become available, such as AmrLib/BoxLib (Rendleman *et al.*, 2000), Chombo (Colella *et al.*, 2007), GrACE (Parashar, 2007), PARAMESH (MacNeice *et al.*, 2000), and SAMRAI (Garaizar, Hornung, and Kohn, 1999). Recent development of the AMR techniques has witnessed the successful applications to MHD problems with disparate spatial and temporal scales (Powell *et al.*, 1999; Linde, 2002; Ziegler, 2008; Stone *et al.*, 2008), among which FLASH (Fryxell *et al.*, 2000; Linde, 2002), PLUTO (Mignone *et al.*, 2007), ATHENA (Stone *et al.*, 2008), NIRVANA (Ziegler, 2008), and BATSRUS (Powell *et al.*, 1999; Tóth *et al.*, 2005, 2012) developed for astrophysics and space-weather modeling are several representatives using oct-tree adaptive meshes.

In the present work, in order to realize the 3D SIP–CESE MHD model on six-component grids (Figure 1) with the AMR capabilities for solar-wind MHD simulations, our considerations run from the points of view of both the grid system with the solar-surface sphere fitting and an easy-to-use AMR implementation. As is well known, our numerical modeling requires the use of the spherical shell domain to describe the computational domain, which leads us to have to treat the lower spherical boundary at the solar surface locating the center of the computational domain. However, dealing with the spherical boundary properly is a critical issue, as the Sun is the source of the activity in the corona and in interplanetary space (Feng, Zhou, and Wu, 2007; Feng *et al.*, 2010; Jiang *et al.*, 2010). In such a spherical-shell computational domain, how to take the advantage of the AMR implementation on a logically Cartesian-structured mesh for a parallel code needs a delicate treatment. Usually, such domains can be partitioned into rectangular or polyhedron mesh grids. If a rectangular box is used, although we can easily implement the AMR with the help of some existing tools such as PARAMESH, CHOMBO, and NIRVANA, we can meet problems in boundary fitting and boundary-condition implementation due to the fact that the spherical surface cannot be consistently described by any rectangular box. To overcome this, the employment of a body-fitted multi-block mesh and cutting-cell method can be a choice, which nevertheless brings the questions of heavy management of the data structure and difficult implementation of the lower spherical boundary conditions, especially for the projected-characteristic method in need of the finite-difference operation on the solar surface (Hayashi, 2005; Wu *et al.*, 2006; Feng *et al.*, 2010). If a polyhedron cell is used (Feng, Zhou, and Wu, 2007; Nakamizo *et al.*, 2009), the sphere and boundary condition can be easily fitted. But for polyhedron grid system, we can encounter difficulties in AMR implementation, since we have no conveniently easy-to-use existing grid-mesh tools or it is too complicated to be ready for use such as OVERTURE at http://www.c3.lanl.gov/cic19/teams/napc/.

Naturally, the Sun's spherical-shaped geometry suggests the use of spherical coordinates (r, θ, ϕ). But spherical-polar grids raise numerical difficulties associated with the presence of both singularities and grid convergence near the poles (Feng *et al.*, 2010), and consequently may negatively impact the accuracy and performance of the numerical procedure. To overcome such problems, some composite or overlapping grids, such as the three-component grid (Usmanov, 1996), the six-component grid (Feng *et al.*, 2010), and the two-component grid (Feng *et al.*, 2011), have been proposed for the numerical study of solar-wind modeling. In the six-component grid mesh (Figure 1), the surface of a sphere is composed of six adjoining grid faces that cover the whole sphere with partial overlapping. The six-component grid faces lend themselves naturally to a multi-component mesh data structure and allow the discretization to be carried out with structured grids, thereby permitting easier implementation of competitive numerical schemes. The 3D six-component grid is obtained by stacking a sequence of concentric 2D spherical shell grids in the radial direction and forming six three-dimensional blocks (Figure 1), each of which is a quadrangular frustum pyramid. The large-scale solar–interplanetary–terrestrial simulation domain decomposition of these meshes can be easily obtained by generating multiple cuts or subdomains in the radial direction, thereby increasing the number of partitioning blocks that can be farmed to different processors to $6N$, where N is the number of cuts. Note that the quasi-uniform and self-similar multi-component nature of the six-component grid makes it ideally suited for implementation on massively parallel architectures (Feng *et al.*, 2010). However, implementing a parallel-AMR approach on the six-component grid system implies a considerable undertaking because most of the AMR software infrastructures are based on a logically Cartesian coordinate. This motivates us to resort to transforming the calculation of the governing PDEs in the physical space to that of associated PDEs in the

reference space (locally or logically Cartesian coordinate), as done by Jiang *et al.* (2010), in order to facilitate the AMR implementation with the help of the PARAMESH toolkit. PARAMESH is an open-source software package of Fortran 90 subroutines and provides us with friendly interfaces to transplant an existing serial code that uses a logically Cartesian structured mesh into a parallel code with adaptive-mesh refinement (AMR) (MacNeice *et al.*, 2000). The same package has been used by the FLASH and ATHENA codes in the broad astrophysics community (MacNeice *et al.*, 2000; Olson, 2006) and is available at http://www.physics.drexel.edu/~olson/paramesh-doc/Users_manual/amr.html.

As the first step, the predictive capabilities of the proposed numerical framework are validated with numerical results for the ambient solar wind for Carrington rotations (CRs) 1967, 2009, 2060, and 2094 obtained on adaptively refined six-component grids through coordinate transformation into the associated reference computational domain. This article is outlined as follows: The governing MHD equations are described in Section 2. Section 3 discusses curvilinear coordinates transformation from physical space to reference space. The AMR strategy is presented in Section 4. Numerical validation of code tests are given in Section 5 for the four CRs. Finally, we present the conclusions and discussions.

2. Governing Equations

The three-dimensional equations governing solar-wind plasma can be described by the following MHD equations in Cartesian coordinates:

$$\frac{\partial \mathbf{U}}{\partial t}+\frac{\partial \mathbf{F}}{\partial x}+\frac{\partial \mathbf{G}}{\partial y}+\frac{\partial \mathbf{H}}{\partial z}-\frac{\partial \mathbf{F}_v}{\partial x}-\frac{\partial \mathbf{G}_v}{\partial y}-\frac{\partial \mathbf{H}_v}{\partial z}=\mathbf{S} \tag{1}$$

where

$$\mathbf{U}=(\rho,\rho v_x,\rho v_y,\rho v_z,e,B_x,B_y,B_z)^{\mathrm{T}},$$

$$\mathbf{F}=\begin{pmatrix}\rho v_x\\ \rho v_x^2+p_0-B_x^2\\ \rho v_x v_y-B_x B_y\\ \rho v_x v_z-B_x B_z\\ (e+p_0)v_x-(\mathbf{v}\cdot\mathbf{B})B_x\\ 0\\ v_x B_y-B_x v_y\\ v_x B_z-B_x v_z\end{pmatrix},\qquad \mathbf{G}=\begin{pmatrix}\rho v_y\\ \rho v_y v_x-B_y B_x\\ \rho v_y^2+p_0-B_y^2\\ \rho v_y v_z-B_y B_z\\ (e+p_0)v_y-(\mathbf{v}\cdot\mathbf{B})B_y\\ v_y B_x-B_y v_x\\ 0\\ v_y B_z-B_y v_z\end{pmatrix},$$

$$\mathbf{H}=\begin{pmatrix}\rho v_z\\ \rho v_z v_x-B_z B_x\\ \rho v_z v_y-B_z B_y\\ \rho v_z^2+p_0-B_z^2\\ (e+p_0)v_z-(\mathbf{v}\cdot\mathbf{B})B_z\\ v_z B_x-B_z v_x\\ v_z B_y-B_z v_y\\ 0\end{pmatrix},$$

$$\mathbf{F}_\mu = \begin{pmatrix} 0 \\ 0 \\ 0 \\ 0 \\ 0 \\ \nu\nabla\cdot\mathbf{B} \\ 0 \\ 0 \end{pmatrix}, \qquad \mathbf{G}_\mu = \begin{pmatrix} 0 \\ 0 \\ 0 \\ 0 \\ 0 \\ 0 \\ \nu\nabla\cdot\mathbf{B} \\ 0 \end{pmatrix}, \qquad \mathbf{H}_\mu = \begin{pmatrix} 0 \\ 0 \\ 0 \\ 0 \\ 0 \\ 0 \\ 0 \\ \nu\nabla\cdot\mathbf{B} \end{pmatrix},$$

$$\mathbf{S} = (0, \rho\mathbf{F}_0, \rho\mathbf{v}\cdot\mathbf{F}_0, \mathbf{0})^{\mathrm{T}} - \nabla\cdot\mathbf{B}(0, \mathbf{B}, \mathbf{v}\cdot\mathbf{B}, \mathbf{v})^{\mathrm{T}} + (0, \mathbf{0}, Q_e, \mathbf{0})^{\mathrm{T}}$$

with the total pressure $p_0 = p + \frac{1}{2}\mathbf{B}^2$. As usual, $e = \frac{p}{\gamma-1} + \frac{1}{2}\rho\mathbf{v}\cdot\mathbf{v} + \frac{1}{2}\mathbf{B}^2$ stands for the total energy density. Here, ρ, $\mathbf{v}$, p, and $\mathbf{B}$ are the mass density, plasma velocity, gas pressure, and magnetic field. We use $\mathbf{j}$ to refer to the electric current density [$\mathbf{j} = (j_x, j_y, j_z) = \nabla\times\mathbf{B}$]. $\mathbf{F}_0$ is the external force exerted on the plasma. γ is the specific-heat ratio and is taken to be 1.5 here.

In Equation (1), the external force $\mathbf{F}_0 = -\frac{GM_s}{r^3}\mathbf{r} - \boldsymbol{\Omega}\times(\boldsymbol{\Omega}\times\mathbf{r}) - 2\boldsymbol{\Omega}\times\mathbf{v}$ is the sum of solar-gravity force and inertial force due to the corotating frame with the Sun. G, M_s, and Ω are the gravity constant, solar mass, and solar angular speed.

In Equation (1), Powell's source terms $-\nabla\cdot\mathbf{B}(0, \mathbf{B}, \mathbf{v}\cdot\mathbf{B}, \mathbf{v})^{\mathrm{T}}$ (Powell *et al.*, 1999) and the diffusive control term $\nabla(\nu\nabla\cdot\mathbf{B})$ (Marder, 1987; van der Holst and Keppens, 2007; Feng *et al.*, 2011) have been added in the MHD equations to deal with the divergence of the magnetic field. Here, following Feng *et al.* (2011), $\nu = 1.3(\frac{1}{\Delta x^2} + \frac{1}{\Delta y^2} + \frac{1}{\Delta z^2})^{-1}$, where Δx, Δy, and Δz are grid spacings in Cartesian coordinates. In our numerical implementation, following Tanaka (1994) we split the full magnetic-field vector [$\mathbf{B}$] into the sum of a time-independent potential magnetic field [$\mathbf{B}_0$] and a time-dependent deviation [$\mathbf{B}_1$], *i.e.* $\mathbf{B} = \mathbf{B}_0 + \mathbf{B}_1$, where $\mathbf{B}_1$ is calculated by the numerical scheme and $\mathbf{B}_0$ is reconstructed with spherical harmonics based on the line-of-sight observations of the photospheric magnetic field. In our AMR implementation of the present article, during the calculation, the values of $\mathbf{B}_0$ on derefined or refined grid points are calculated from the spherical harmonics. However, the time-dependent part $\mathbf{B}_1$ is involved in the updating procedure. It is generally believed that solving for the deviation $\mathbf{B}_1$ from the embedded field $\mathbf{B}_0$ is inherently more accurate than solving for the full magnetic-field vector $\mathbf{B}$ (Gombosi *et al.*, 2003; Nakamizo *et al.*, 2009; Feng *et al.*, 2010, 2011). Indeed, in our validation tests of the present article, these numerical techniques enable us to maintain the $\nabla\cdot\mathbf{B}$ error to an acceptable level of 10^{-6} and to avoid negative pressure during the calculation.

The primitive variables ρ, $\mathbf{v}$, p, $\mathbf{B}$, r, and t in these equations are normalized by the characteristic values ρ_s, a_s, $\rho_s a_s^2$, $\sqrt{\rho_s a_s^2}$, R_s, and R_s/a_s, where ρ_s and a_s are the density and ion–acoustic wave speed at the solar surface. Solar rotation is considered in the present study with angular velocity $|\boldsymbol{\Omega}| = 2\pi/27.2753$ radian day^{-1} (normalized by a_s/R_s in simulations). A factor of $1/\sqrt{\mu}$ has been absorbed into the definition of $\mathbf{B}$.

In order to achieve the observed pattern of fast and slow solar winds through MHD simulations, researchers often add various kinds of heating terms into the MHD models. The most commonly used heating methods are the Alfvén wave heating with Wentzel–Kramers–Brillouin approximation, turbulence heating and volumetric heating. The Alfvén wave heating method uses the idea of the energy and momentum interchange between the solar plasma and the large-scale Alfvén turbulence to heat and accelerate the solar wind (*e.g.*, Mikić *et al.*, 1999; Usmanov, 1996; van der Holst *et al.*, 2010; Riley *et al.*, 2011). The turbulence heating method assumes that the additional energy is stored in the turbulent internal degrees of freedom, which is realized by using a phenomenological, thermodynamic

model with a varied polytropic index (*e.g.* Roussev *et al.*, 2003; Cohen *et al.*, 2008; van der Holst *et al.*, 2010). In the volumetric heating method, the deposition of energy and/or momentum into the solar wind has been described by means of some empirical source terms without explicitly specifying the physical mechanisms (*e.g.* Nakamizo *et al.*, 2009; Lionello, Linker, and Mikić, 2009; Feng *et al.*, 2010). Here, the energy-source term Q_e in the energy equation adopts the volumetric heating method, which is formulated in Feng *et al.* (2010) with the help of the Wang–Sheeley–Arge (WSA) model (Wang and Sheeley, 1990; Arge and Pizzo, 2000; Arge *et al.*, 2003). This energy-source term takes account of the flux-tube expansion factor [f_s] and the minimum angular separation (at the photosphere) between an open-field foot point and its nearest coronal hole boundary [θ_b, measured in degrees], which have been used for the solar-wind study (Owens *et al.*, 2008; Nakamizo *et al.*, 2009; Taktakishvili *et al.*, 2011).

The solar-wind evolution is calculated in coordinates corotating with the Sun. In this coordinate system we use (r, θ, ϕ) for the position of a point in solar-interplanetary space and (x, y, z) is used to express its corresponding Cartesian coordinates, and the Cartesian coordinates (x, y, z) and its corresponding spherical coordinates (r, θ, ϕ) will be referred to alternatively. Sometimes, the analysis of computational results is carried out in the coordinate system at rest in order to compare with the observations.

The calculations are performed between 1 R_s (*i.e.* the base of the corona) and 328 R_s. The initial solar-surface temperature and number density are 1.3×10^6 K and 2.0×10^8 cm^{-3}. We employ the projected-normal characteristic inner boundary condition combined with the mass flux escaping through the solar surface (Hayashi, 2005). Then the code is initialized by using the potential magnetic field based on the line-of-sight measurements of the photospheric magnetic field from the Wilcox Solar Observatory (WSO) at Stanford University for the CRs of interest and the Parker solar-wind solution. Finally, our model is run using a time-relaxation method until a quasi-steady state is achieved. In fact, the same boundary conditions and initial conditions given in Section 5 of Feng *et al.* (2010) are observed in the present article.

The SIP–CESE MHD model has been developed by us in a series of articles (Feng, Zhou, and Wu, 2007; Feng *et al.*, 2010). Very recently, the CESE method for the MHD equations in general curvilinear coordinates has been proposed and validated for some pure MHD benchmark problems (Jiang *et al.*, 2010). For the present article to be self-contained, in what follows we present the main points of six-component grid and curvilinear coordinate transformation from physical to reference coordinates in the context of solar-wind modeling.

3. Six-Component Grid and Curvilinear Coordinate Transformation

This section is devoted to the curvilinear coordinate transformation and six-component grid in both physical space and reference space, where our CESE solver is applied. The six-component grid introduced by Feng *et al.* (2010) for the solar-wind study decomposes the spherical-shell computational domain into six identical component meshes with partial overlapping regions (Figure 1), each component of which is identically defined by a low-latitude spherical domain

$$\left(\frac{\pi}{4} - \delta \le \theta \le \frac{3\pi}{4} + \delta\right) \cap \left(\frac{3\pi}{4} - \delta \le \phi \le \frac{5\pi}{4} + \delta\right).$$

The parameter $\delta = \Delta\theta$ is determined by the grid spacing and layers of guard cells required for the minimum overlapping area of two grid sizes. It should be mentioned that in 3D

solar-wind modeling, Usmanov (1996) also introduced a composite mesh with the two polar caps replaced by a rotated spherical grid. His composite mesh consists of three overlapping spherical meshes. The first one is the usual spherical mesh with a limited extent in latitude ($42 \le \theta_1 \le 138°, 0 \le \phi_1 \le 360°$). The polar axis of the mesh is directed along the solar-rotation axis. Two other meshes are introduced to cover the polar regions in both hemispheres. These meshes are fragments of spherical coordinates ($36 \le \theta_{2,3} \le 144°, 26 \le \phi_2 \le 144°$, and $216 \le \phi_3 \le 324°$) with the polar axis laying in the equatorial plane of the first coordinate system ($\theta_1 = 90°, \phi_1 = 90°$). The differences between Usmanov's composite grid and six-component grid are that the six-component grid partitions the spherical shell into six identical regions with the same metric and the component grids can be transformed into each other by coordinate transformation such that the basic equations, numerical grid distribution, and all numerical tasks are identical in the computational space. These attributes are convenient to make efficient and concise programs and speed up the calculation. Different from other grid mesh on which a numerical scheme is built, the six-component grid is just the projection of our space–time grid system for the CESE scheme (Feng, Zhou, and Wu, 2007).

Actually, we use a six-component grid system in the physical space and each component deals with the same grids, basic equations, and numerical tasks. Hence we do not have to distinguish them and we only need to describe the grid partition and the associated coordinate transform. Keep in mind that our physical space is in Cartesian coordinates (x, y, z) or corresponding spherical coordinates (r, θ, ϕ) or solution variables defined in them, and we will refer to them without distinguishing. In both θ and ϕ directions, the grid points are even spaced such that $\Delta\theta = \Delta\phi$. However, in the r direction, a new variable λ is introduced as a reference coordinate in reference space, which is exponentially related with r by $r = a^\lambda, a = 1.481$. In this way, the grid spacing $[\Delta r]$ in the r direction is always around $r\Delta\theta$ and $r \sin\theta \Delta\phi$ ($\Delta\theta$ is already chosen to be equal to $\Delta\phi$) by choosing $\Delta\lambda = \log_a(1 + \Delta\theta)$, so that each grid cell is always approximately a cube. The $\sin\theta$ term varies from 1 to $1/\sqrt{2}$ within the six grid components, which shows that avoiding the singularity of the spherical grid indeed results in more regular cells. Thus, the curvilinear or reference coordinates (ξ, η, ζ) used in our CESE solver refer to (λ, θ, ϕ) here. Meanwhile, the grid cell in the reference space (ξ, η, ζ) is a rectangular box. In principle, any parameter $a > 1$ can be chosen. In order to make the cells more regular in the physical space, we only need to choose $\Delta\lambda = \log_a(1 + \Delta\theta)$ such that $\Delta r = a^\lambda(a^{\Delta\lambda} - 1) = r\Delta\theta$. We have no preference for selecting the parameter a, but the larger the parameter a, the denser the grid in the reference space, which makes no difference due to the AMR implementation. We have tested many cases for such a choice $a \in [1.2, 3]$, but have seen no difference in the numerical results. The choice $a = 1.481$ is just a representative case for presenting our results here.

Initially, the computational domain in every reference component is divided into $14 \times 4 \times 4$ blocks with each block consisting of $6 \times 6 \times 6$ cells. These correspond to $N_\theta = N_\phi = 25$ and $\Delta\theta = \pi/48$ by defining gird points on each component in physical space as $\theta_j^\ell = \theta_{\min} + j\Delta\theta, j = 0, 1, \ldots, N_\theta + 1, \phi_k^\ell = \phi_{\min} + k\Delta\phi, k = 0, 1, \ldots, N_\phi + 1$ and $\Delta\theta = (\theta_{\max} - \theta_{\min})/(N_\theta - 1), \Delta\phi = (\phi_{\max} - \phi_{\min})/(N_\phi - 1)$, where N_θ and N_ϕ are the mesh numbers of the latitude and longitude, respectively. $\theta_{\min} = \frac{\pi}{4}, \theta_{\max} = \frac{3\pi}{4}, \phi_{\min} = \frac{3\pi}{4}, \phi_{\max} = \frac{5\pi}{4}$. The innermost region is set on the solar surface at 1 R_s and the outermost region on the sphere at 328 R_s, such that each component of the physical grids is equivalent to $0 \le \xi \le 14.75$, $\pi/4 - \delta \le \eta \le 3\pi/4 + \delta$, and $3\pi/4 - \delta \le \zeta \le 5\pi/4 + \delta$ in the computational domain or reference space, with $\Delta\xi = \log_a(1 + \Delta\theta)$, and $\Delta\eta = \Delta\zeta = \delta = \Delta\theta = \frac{\pi}{48}$. To be specific,

the transformation [**J**] between the coordinates of the reference space and the physical space for one component reads as follows:

$$\begin{cases} x_1 = a^{\xi} \sin\eta \cos\zeta \\ y_1 = a^{\xi} \sin\eta \sin\zeta \\ z_1 = a^{\xi} \cos\eta \end{cases}, \qquad \begin{cases} \xi = \log_a \sqrt{x_1^2 + y_1^2 + z_1^2} \\ \eta = \arccos\left(z_1 / \sqrt{x_1^2 + y_1^2 + z_1^2}\right) \\ \zeta = \arctan(y_1 / x_1) \end{cases}. \tag{2}$$

which will be denoted by $x = x(\xi, \eta, \zeta)$, $y = y(\xi, \eta, \zeta)$, $z = z(\xi, \eta, \zeta)$ or $\xi = \xi(x, y, z)$, $\eta = \eta(x, y, z)$, $\zeta = \zeta(x, y, z)$. The Jacobian matrix of this nonsingular curvilinear coordinate transform **J** is written as

$$\mathbf{J} = \frac{\partial(x, y, z)}{\partial(\xi, \eta, \zeta)} = \begin{pmatrix} a^{\xi} \sin\eta \cos\zeta \ln a & a^{\xi} \cos\eta \cos\zeta & -a^{\xi} \sin\eta \sin\zeta \\ a^{\xi} \sin\eta \sin\zeta \ln a & a^{\xi} \cos\eta \sin\zeta & a^{\xi} \sin\eta \cos\zeta \\ a^{\xi} \cos\eta \ln a & -a^{\xi} \sin\eta & 0 \end{pmatrix}, \tag{3}$$

and its determinant is $J = |\mathbf{J}| = a^{3\xi} \sin\eta \ln a$.

With the transformations (2), (3), and those of variables between components (Feng *et al.*, 2010; Jiang *et al.*, 2010), we can get the corresponding transformation of coordinates between any two components or transformation of solution vector variables between the reference space and the physical space on an arbitrary component. The 3D MHD equations of solar-wind plasma (1) in the reference coordinates (ξ, η, ζ) read

$$\frac{\partial \hat{\mathbf{U}}}{\partial t} + \frac{\partial \hat{\mathbf{F}}}{\partial \xi} + \frac{\partial \hat{\mathbf{G}}}{\partial \eta} + \frac{\partial \hat{\mathbf{H}}}{\partial \zeta} - \frac{\partial \hat{\mathbf{F}}_v}{\partial \xi} - \frac{\partial \hat{\mathbf{G}}_v}{\partial \eta} - \frac{\partial \hat{\mathbf{H}}_v}{\partial \zeta} = \hat{\mathbf{S}}, \tag{4}$$

where $\hat{\mathbf{U}}$, $\hat{\mathbf{F}}$, $\hat{\mathbf{G}}$, $\hat{\mathbf{H}}$, $\hat{\mathbf{F}}_v$, $\hat{\mathbf{G}}_v$, $\hat{\mathbf{H}}_v$, and $\hat{\mathbf{S}}$ are given in Equation (21) by Jiang *et al.* (2010).

Note that Equation (4) is still written in conservation form, just like Equation (1). As a result, the CESE solver for Equation (4) in the reference coordinate space (ξ, η, ζ) can be derived in the same way as that for Equation (1) according to Jiang *et al.* (2010). It should be noted that transforming the governing equations of conservation laws into curvilinear coordinates or new coordinates have been derived and used in constructing numerical algorithms for years (*e.g.* Vinokur, 1974; Bridges, 2008). Here, we rewrite it again just for the convenience of description.

With the CESE solver for both Equation (1) and Equation (4), we can easily take turns between the physical-solution variables and the reference-solution variables. If the initial input of the physical solution variables is given, we first use **F**, **G**, **H**, **S** to calculate the fluxes $\hat{\mathbf{F}}$, $\hat{\mathbf{G}}$, $\hat{\mathbf{H}}$, $\hat{\mathbf{S}}$ and apply the CESE solver to Equation (4) to obtain the reference-solution variables $\hat{\mathbf{U}}$ and their first-order derivatives $(\hat{\mathbf{U}}_{\xi}, \hat{\mathbf{U}}_{\eta}, \hat{\mathbf{U}}_{\zeta})$ at the new time step. Finally, we can recover the physical solution variables **U**. Of course, we can reverse the above process from the reference-solution variables to the physical-solution variables.

It is evident that the only difference between the CESE solver in Cartesian coordinates and reference coordinates is the coordinate transformation **J**, and consequently the same solver applies to both grid systems. Meanwhile, the present CESE solver in the reference space (ξ, η, ζ), formulated through the curvilinear transform from the physical space to the reference space, solves the transformed MHD equations with rectangular box cells in a logically Cartesian space, and the treatment of time iteration by integrating two half timesteps into one full timestep can be seen as a one-step update that leads to low storage and makes the scheme suitable building blocks for adaptive-mesh refinement calculations. These advantages greatly simplify the effective realization of numerical methods and allow us to easily carry out the AMR implementation with the help of PARAMESH.

4. AMR Implementation of SIP–CESE MHD Model

Here, we present some details of the AMR implementation of the SIP–CESE MHD model on the six-component grid system (Figure 1) of the spherical-shell domain in solar-terrestrial space. To accomplish this, all the ranks are classified into six groups, each of which corresponds to one component grid system and deals with the same grid, basic equations, and numerical task. Since our AMR is realized in the reference space (ξ, η, ζ) and one component grid in the physical space corresponds to one associated reference component gird, the PARAMESH package decomposes every reference component (*i.e.*, our computational space) into many blocks of the same size, and organizes all the blocks in the whole computational space (patched by the six reference components) into an oct-tree structure. In our implementation, we store both the solution variables and their first-order derivatives $[\hat{\mathbf{U}}, \hat{\mathbf{U}}_\xi, \hat{\mathbf{U}}_\eta, \hat{\mathbf{U}}_\zeta]$ at each solution point, which have the number of variables $\mathsf{nvf} = 4 \times 8 = 32$. The block size is set to $6 \times 6 \times 6$ cells, with one layer of guard cells containing diagonal elements. PARAMESH manages all the rectangular blocks, and does not need to distinguish which group the blocks belong to, such that we can directly use most of the default operations provided by PARAMESH, such as the refining or coarsening of the blocks, prolongation, and restriction. Therefore, the data transferring and guard cell filling between blocks can be automatically accomplished by the package without large modification. In practice, the data exchange between these blocks in the same component is completed by PARAMESH. However, the data exchange at overlapping layers between different components adopt the third-order Lagrange interpolation. This, of course, will sacrifice the conservation at the component interfaces. We have tested the code with a dipole, multiple magnetic field and the observed magnetic field used in the present article as input to find that no spurious reflections are observed from the grid interface. This may be due to the fact that the conservative properties are more important to model shock waves either due to coronal mass ejections (CMEs) or corotating interaction regions (CIRs) than to model smooth solar wind.

In solar-wind modeling, the topology of heliospheric current sheet is an important structure and thus only the curl of the magnetic field is used as our refinement strategy to capture the current sheet. The standard deviation about zero $[\tau_e = \sqrt{\sum_{i=1}^{N} \chi_{e_i}^2 / N}]$ is computed for $\chi_e = V^{0.5} \frac{|\nabla \times \mathbf{B}|}{|\mathbf{B}| + \epsilon \sqrt{\rho}}$ and $\epsilon = 10^{-10}$ to set the thresholds of refining and coarsening grid (De Zeeuw, 1993), with V being the spatial cell volume. When the maximum of this criterion in a block is greater than $\kappa \tau_e$, this block is flagged to be refined, while if the maximum in a block is less than $\varsigma \tau_e$, this block is flagged to be coarsened. κ and ς are selected according to different physical time [t_H in units of hours] intervals during the code's running. That is, when $t_H < 20$, $\kappa = 3$ and $\varsigma = 0.1$; when $20 \le t_H < 50$, $\kappa = 6$ and $\varsigma = 0.2$; when $50 \le t_H < 100$, $\kappa = 10$ and $\varsigma = 0.3$; when $100 \le t_H < 160$, $\kappa = 15$ and $\varsigma = 0.4$; and when $t_H \ge 160$, $\kappa = 6$ and $\varsigma = 0.1$. With these settings, nine levels of grid refinement are used to obtain a grid cell size of 0.015 R_s on the solar surface. The grid throughout the simulation is refined to obtain a grid cell size of about 0.15 R_s near the current sheet within 20 R_s and it is about 0.7 R_s near 1 AU. The maximum grid cell size is 1.3 R_s in the corona and 7 R_s in the inner heliosphere.

As argued by Feng *et al.* (2010), the multiple time-stepping algorithm is implemented in a six-component grid system with the radial direction decomposed into six subdomains: 1 – 10 R_s, 10 – 20 R_s, 20 – 50 R_s, 50 – 100 R_s, 100 – 170 R_s, and 170 – 328 R_s. Each subdomain corresponds to one time step. We first calculate the smallest time step $[\Delta t_{\min}]$ in the whole domain. Then the smallest time step in each subdomain $[\Delta t_q]$ is calculated. The time step for each block in each subdomain $[\Delta t_b]$ is taken to be the same as $\Delta t_b = 2^{\mathrm{int}(\log_2(\Delta t_q / \Delta t_{\min}))} \times \Delta t_q$. Finally, all of the blocks are advanced as done by Jiang *et al.* (2010).

5. Numerical Validations

In this section, we will demonstrate the capability of the newly established 3D SIP–AMR–CESE MHD solar-wind model to reproduce the observations both near the Sun and in interplanetary space during different solar-activity phases. The selected time intervals are Carrington rotation (CR) 1967 from 23:30 UT (universal time) on 02 September to 05:57 UT on 30 September 2000, CR 2009 from 13:03 UT on October 23 to 20:20 UT on 19 November 2002, CR 2060 from 14:20 UT on 14 August to 20:18 UT on 10 September 2007, and CR 2094 from 04:08 UT on 27 February to 11:44 UT on 26 March 2010. The four CRs belong to the solar maximum, declining, minimum, and rising phases in Solar Cycles (SCs) 23 and 24, respectively, according to the monthly sunspot numbers, which are available at http://solarscience.msfc.nasa.gov/greenwch/spot_num.txt.

5.1. Comparisons with the Observation Near the Sun

Figure 2 presents the synoptic maps of the coronal holes from both observations and simulations for CR 1967 (Column a), CR 2009 (Column b), CR 2060 (Column c), and CR 2094 (Column d). The first row presents the synoptic observations of the solar surface at 195 Å taken with the *Extreme ultraviolet Image Telescope* (EIT) onboard *Solar and Heliospheric Observatory* (SOHO), where coronal holes appear as dark areas of weaker coronal emission due to lower density and temperature (Harvey and Recely, 2002). The second row shows the open-field and closed-field regions from the SIP–AMR–CESE MHD model.

It is generally accepted that the areas and the distributions of the coronal holes are different in different solar-activity phases. Seen from the observation and the simulation in CR 1967, no polar coronal holes (PCHs) appear at either pole. In fact, this is one of the most significant features before the completion of the reversal of the polar field during solar-maximum phases (Waldmeier, 1981; Harvey and Recely, 2002; Bilenko, 2002). Only a few isolated coronal holes (ICHs) scatter around Carrington longitudes of $\phi = 10°$, $100°$, $180°$, and $270°$ at the low- and middle-heliographic latitudes. We should note that the simulated locations of the ICHs are roughly in agreement with the observed ones but the total area of the ICHs from the simulation is a little smaller than that from measurements. For CR 2009, in the declining phase, the EIT observation and the calculation reveal that the PCHs tend to be asymmetric about both poles and that the two PCHs extend equatorward across the solar Equator. The latitudinal median for the equatorial boundaries of PCHs excluding the extending holes is about $74°$, and the lowest latitude is about $-10°$ for the northern extending hole and $10°$ for the southern one. In CR 2060, the Sun was at its minimum phase. The northern and southern PCHs are nearly symmetric about both poles. In addition, two small ICHs appear near the solar Equator around $\phi = 230°$ and $350°$ from both the observations and simulation, which was rare during previous solar minima and was investigated thoroughly (*e.g.* Tokumaru *et al.*, 2009; Wang, Robbrecht, and Sheeley, 2009; Yang *et al.*, 2011; Abramenko *et al.*, 2010). Additionally, corona holes occupy the largest area in the four selected CRs, which agrees with the finding of Harvey and Recely (2002). The locations of the coronal-hole boundaries are almost the same as those derived from the model of potential-field source-surface (PFSS) based on the photospheric magnetograms of Mount Wilson Solar Observatory (Luhmann *et al.*, 2009). With the end of the extended solar minimum came the rising phase of SC 24. In CR 2094, both PCHs from the simulation and observation shrink poleward rapidly and the simulated latitudinal median for the equatorial boundaries of PCHs moves poleward from about $63°$ in CR 2060 to $68°$ in CR 2094.

Associated with the differences in shapes and areas of the coronal holes on the solar surface among the four selected CRs, there also exist some corresponding distinctions near

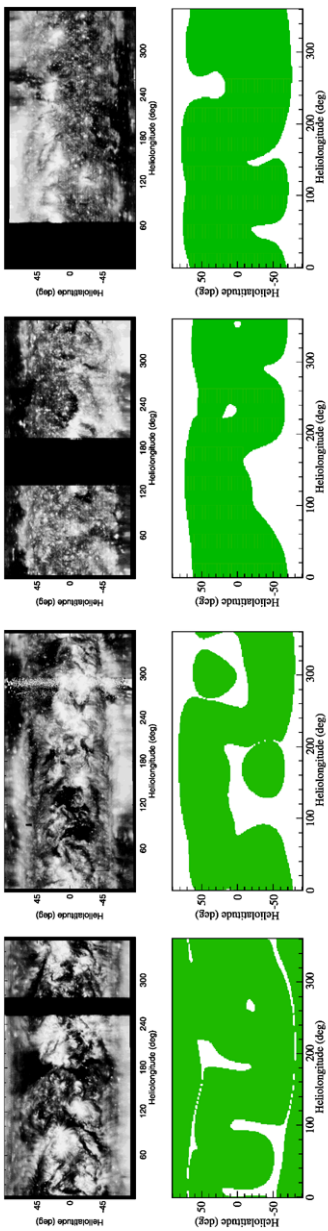

Figure 2 Synoptic maps of the coronal holes at 1 R_S for CR 1967 (Column a), CR 2009 (Column b), CR 2060 (Column c), and CR 2094 (Column d). The first row is the SOHO/EIT 195 Å observation, in which the black vertical stripes represent data gaps. The second row presents the open-field regions and closed-field ones from the SIP–AMR–CESE MHD model, where the green shaded areas are of a closed magnetic field and the white regions are of an open field.

the Sun among them. Figure 3 shows the measured and computed synoptic maps at 2.5 R_s for CR 1967 (Column a), CR 2009 (Column b), CR 2060 (Column c), and CR 2094 (Column d). The first and second rows are the white-light polarized brightness (pB) images at the east and west limbs from the *Large Angle Spectrometric Coronagraph* (LASCO) C2 onboard SOHO. Each image in the third row superimposes the isolines of the radial magnetic field on the contour map of the simulated number density $[N]$ and the fourth row shows the contour maps of the radial speed $[v_r]$. In Row 4, the black solid lines denote the magnetic neutral lines (MNLs). The most significant differences among the four CRs shown in Figure 3 include the topologies of the MNLs and the distributions of the low-density, high-speed (LDHS) plasma flows. In the simulation for CR 1967, the MNL along the longitudes from 330° through 0° to 120° is almost coincident with the latitudinal circle of 60° N except that there is a dip around 40° longitude and the MNL along the longitudes from 160° to 300° lies at the latitude of 60° S. As a result, the MNL around the longitudes of 130° and 320° is nearly vertical and the heliosphere at low and middle latitudes is divided into two unipolar regions according to the IMF polarities. The latitudes of the MNL from the simulation are slightly smaller than those derived from *Ulysses*' crossings of the sector structure when it traveled from 80.2° S to 70° N (Smith *et al.*, 2003, 2011). In addition, the LDHS regions are confined to the small areas in the neighborhood of the longitudes of 0°, 100° and 200° and the high-density, low-speed regions spread widely, which is in agreement with *Ulysses* solar-wind observations (McComas *et al.*, 2002, 2003). Therefore, the bright features can be observed almost everywhere from the synoptic maps of pB measurements. However, the bright structures in the pB map recorded in CR 2009 are roughly distributed around the computed MNL, which lies at about 40° N from $\phi = 60°$ to 300° and 40° S from 240° to 20°, and changes abruptly near the longitudes of 40° and 220°. It is obvious that the dark regions in the pB maps are consistent with the distribution of calculated LDHS plasma flows, which not only cover both poles, but also occupy the low- and middle-latitude regions around the longitudes of 0°, 100°, and 200°. The latitudinal span of the high-density, low-speed solar wind is compatible with the measurements of solar-wind speed by *Ulysses* during this CR (McComas *et al.*, 2006). For CR 2060, the brightest streaks at both limbs in the pB maps from LASCO-C2 are well organized around the wavy MNL, which is confined to low latitudes near the solar Equator and extends northward to 25° N at $\phi = 160°$ and southward to 15° S at $\phi = 230°$. Additionally, the percentage of the LDHS regions is highest among the four CRs. As far as CR 2094 is concerned, the bright features in LASCO-C2 observations can be seen at very broad latitudes due to the complex structure of the MNL, which displays a pattern of two peaks and two valleys seen from the simulation. The two peaks are located at $(\theta, \phi) = (35°, 70°)$ and $(35°, 160°)$. The narrow valley is located at $(-25°, 100°)$ and the wide one at $(-30°, 260°)$. The median of equatorial boundaries for the LDHS plasma flows from unipolar PCHs is about the latitude of 50° excluding the extending part of northern PCH in the wide trough.

Now we investigate the states of the solar wind from 2.5 to 6 R_s. Figure 4 displays the coronal observations and the simulated results for CR 1967 (Column a), CR 2009 (Column b), CR 2060 (Column c), and CR 2094 (Column d). The first four rows extract the computed results on the meridional plane at $\phi = 0° - 180°$ and some related observations. The first and second rows are the white-light pB images from 2.3 to 6 R_s recorded by SOHO/LASCO-C2 and computed from the simulation, respectively. The LASCO-C2 data are available at http://sharpp.nrl.navy.mil/cgi-bin/swdbi/lasco/img_short/form. The third row is the simulated magnetic-field topologies projected on the meridional planes from 1 to 6 R_s. The fourth row is the simulated radial solar-wind speed on the meridional plane from 1 to 6

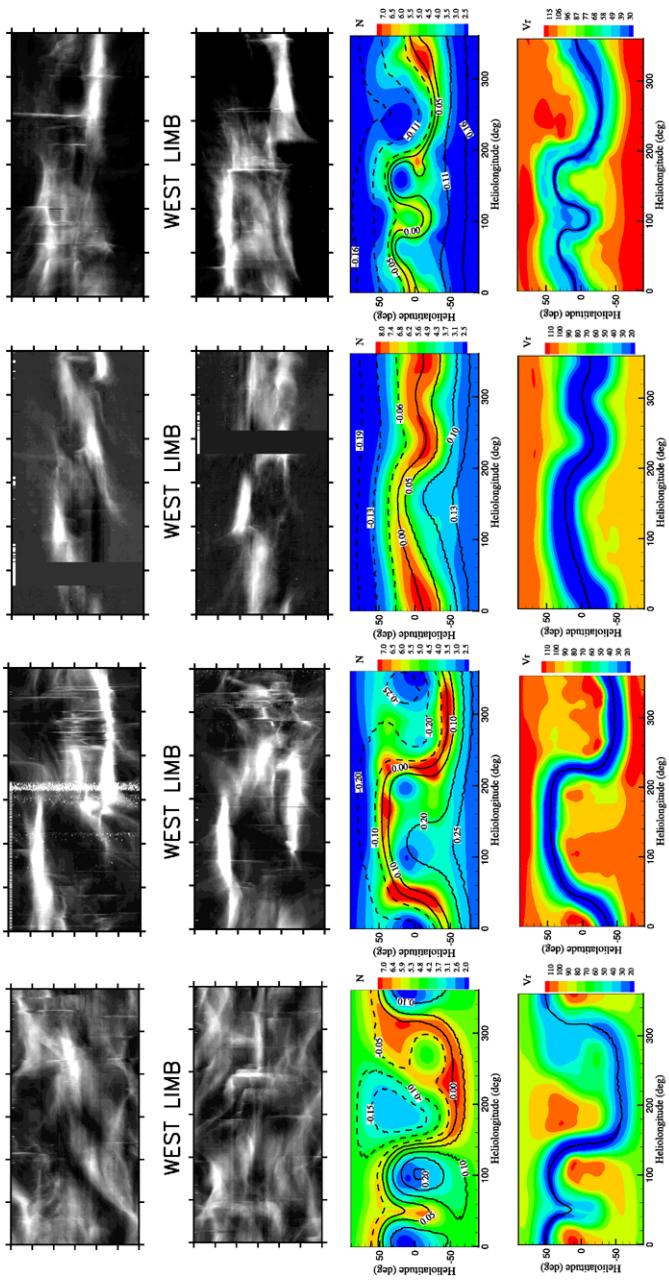

Figure 3 Synoptic maps at 2.5 R_s for CR 1967 (Column a), CR 2009 (Column b), CR 2060 (Column c), and CR 2094 (Column d). The first and second rows are the white-light polarized brightness at the east and west limbs from SOHO/LASCO-C2. The third row overlays the isolines of the radial magnetic field [Gauss] on the contour maps of the simulated number density N [10^5 cm^{-3}] and the fourth rows are the pseudo-color images of the radial speed v_r [km s^{-1}]. In Row 3, the dashed lines stand for an inward radial magnetic field and the solid ones for an outward radial magnetic field. The black lines in the last row denote the magnetic neutral lines.

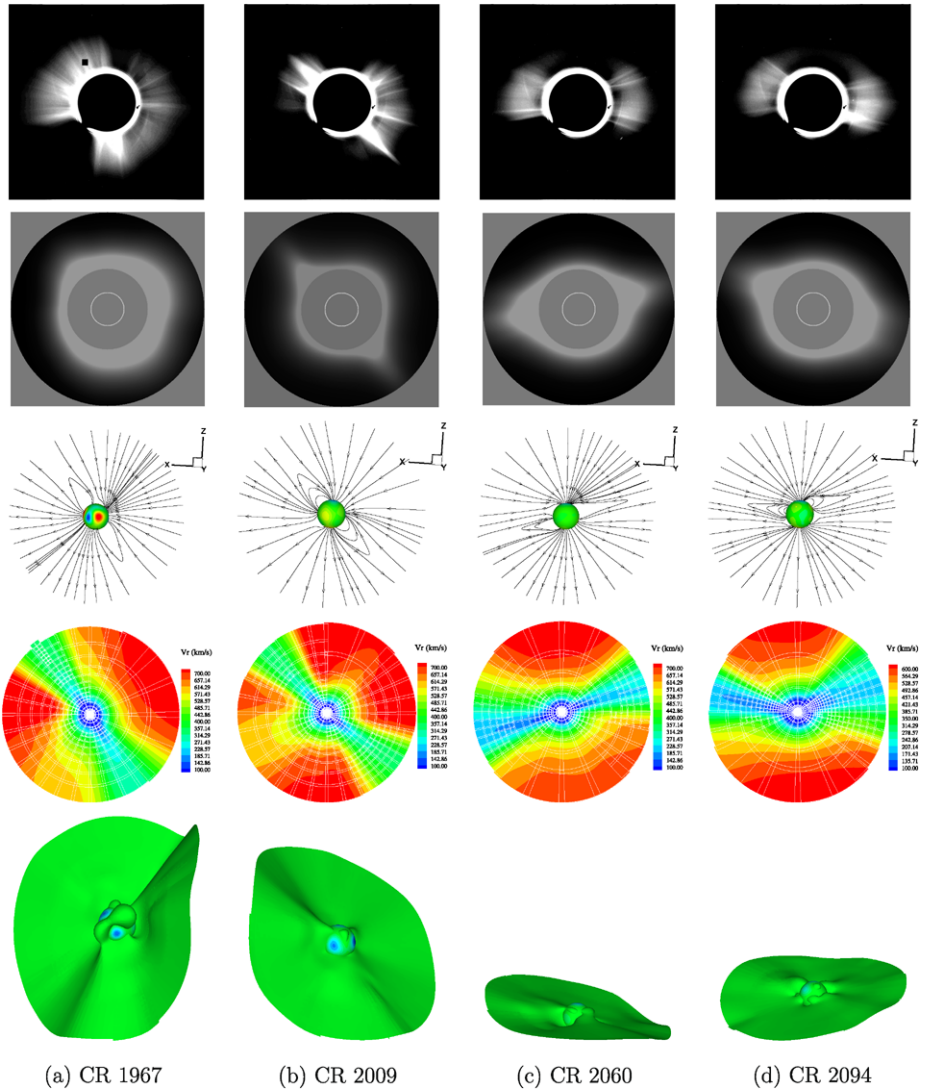

Figure 4 The coronal observations and the simulation results on the meridional plane at $\phi = 0° - 180°$ for CR 1967 (Column a), CR 2009 (Column b), CR 2060 (Column c), and CR 2094 (Column d). The first and second rows are the white-light pB images from 2.3 to 6 R_S recorded by SOHO/LASCO-C2 and computed from the simulation, respectively. The third row is the simulated magnetic-field topology projected on the meridional planes from 1 to 6 R_S. The fourth row is the simulated radial solar-wind speed on the meridional planes from 1 to 6 R_S, where the white quadrilaterals denote the grid blocks. The last row exhibits the simulated current sheets from 1 to 6 R_S.

R_S, where the white quadrilaterals represent the blocks of different refinement levels showing that the regions near the current sheet are identified by the grid resolution. The last row exhibits the simulated three-dimensional current sheets from 1 to 6 R_S.

In CR 1967, the bright streaks extend at almost all latitudes in the images for both the numerical results and the observations and the dark area in the southeast quadrant in the

C2 observation results from the occulter's pylon of the telescope. The brightest structures extending farthest in CR 2009 lie just in the simulated streamers because most regions are covered with the LDHS plasma flows, which can be clearly seen from the simulation. For CR 2060, the current sheet is concentrated on the solar Equator and of limited latitudinal excursion. The HCS during this period can be approximated as a flat plane, although the HCS is not as conventional as those in previous minima (Tokumaru *et al.*, 2009; Yang *et al.*, 2011) and slow solar winds span more latitude so that the spacecraft near the Earth sampled fewer high solar-wind flows (Luhmann *et al.*, 2009). Past studies have also revealed the different shapes of HCS in different solar-activity phases. The HCS in the solar maximum extends to very high latitudes (*e.g.* Cohen *et al.*, 2008) and the HCS in the solar minimum is almost coincident with the solar Equator (*e.g.* Mikić *et al.*, 1999; Cohen *et al.*, 2008; Feng *et al.*, 2010; van der Holst *et al.*, 2010; Riley *et al.*, 2011). During CR 2094, we can find that the bright fan-like structures cover low and middle latitudes in both the observed and synthesized pB images, and that the current sheet fluctuates with relatively large amplitude and cannot be described as a nearly flat plane any more, which is similar to the simulated HCS structure of CR 1934 by Mikić *et al.* (1999). We also notice that the solar-wind speeds at six solar radii in our simulations are higher than those in van der Holst *et al.* (2010), which probably results from the major acceleration region for our simulation being a little closer to the Sun than that of the model by van der Holst *et al.* (2010).

5.2. Comparison with the Observation in Interplanetary Space

After discussing the coronal states of the four CRs near the Sun, we turn our attention to the comparison between the simulated and observed results in interplanetary space.

The first row in Figure 5 displays the composite images of the isolines for the radial speed [v_r] and the pseudo-color images of the mass-flux density [F_m] escaping through the surface at 20 R_s. Row 2 displays the steady solutions in the solar equatorial plane for the selected four CRs, and the white quadrilaterals suggest that the blocks of higher refinement levels are clustering near the low-speed region, which means that the current-sheet structure is well captured by the adaptive meshes. Rows 3 and 4 show the simulated proton number densities [N] and v_r at 215 R_s. Columns (a), (b), (c), and (d) correspond to the results for CRs 1967, 2009, 2060, and CR 2094. In those maps, the dashed green lines in the first row and the black solid lines in the third and last rows denote the magnetic neutral lines.

Comparing Figures 3 and 5, we can see that for all the four CRs, the plasma flows of $v_r \geq 60\ \mathrm{km\,s^{-1}}$ at 2.5 R_s have been accelerated to the intermediate-speed solar winds (ISWs, $450 \leq v_r \leq 700\ \mathrm{km\,s^{-1}}$) or fast solar winds (FSWs, $v_r \geq 700\ \mathrm{km\,s^{-1}}$) of low mass-flux density at 20 R_s and the slow solar winds (SSWs, $v_r \leq 450\ \mathrm{km\,s^{-1}}$) at 20 R_s of high density basically surrounding the HCS originate from the plasma flows of $v_r \leq 60\ \mathrm{km\,s^{-1}}$ at 2.5 R_s. As a result, FSW covers the smallest area in CR 1967 and the largest in CR 2060. In addition, all SSW, ISW, and FSW have experienced an acceleration of about $\approx 50-100\ \mathrm{km\,s^{-1}}$ from 20 R_s to 215 R_s. The radial variations of the acceleration for different types of solar wind beyond 2.5 R_s are consistent with those derived from both *Ulysses* solar-corona experiment (Pätzold, Tsurutani, and Bird, 1997) and LASCO-C2 and C3 measurements (Wang and others, 1998; Porfir'eva *et al.*, 2009). The values of the mass-flux densities and solar-wind speeds are of the same magnitude as those given by Wei *et al.* (2003), who analyzed the global distribution of coronal mass output at 2.5 R_s and its relation to solar magnetic-field structures by using observational data from K-coronal brightness. Additionally, the results have also revealed the longitudinal deflections of the solar wind due to solar rotation and the freezing-in effect of interplanetary magnetic field (IMF) by comparing the shapes of HCSs

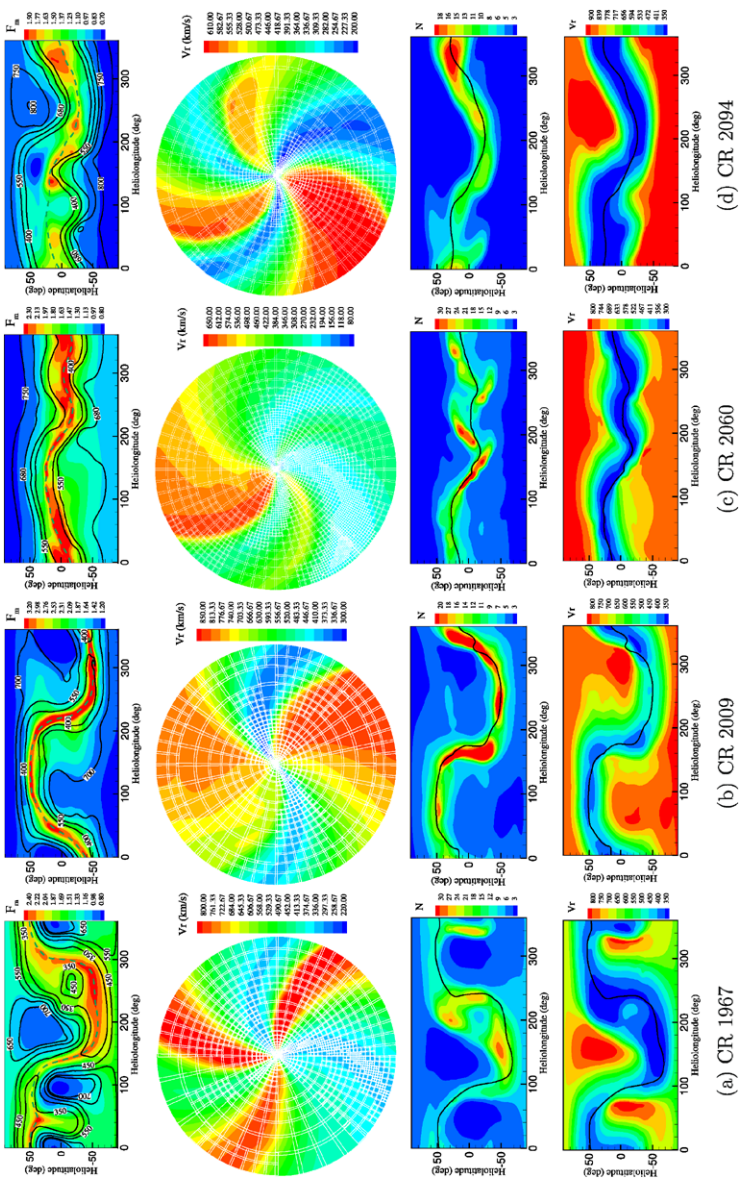

Figure 5 The simulated steady solution in interplanetary space from the MHD model for CR 1967 (Column a), CR 2009 (Column b), CR 2060 (Column c), and CR 2094 (Column d). The isolines of the radial speed [v_r: $\mathrm{km\,s^{-1}}$] superimposed on the synoptic pseudo-color image of the mass-flux density [F_m: $10^8\ \mathrm{km\,s^{-1}\ cm^{-3}}\ R_S^2$] at 20 R_S (Row 1), the pseudo-color images of the radial velocity in the solar equatorial plane (Row 2), the synoptic contours of the simulated proton number density [N: $\mathrm{cm^{-3}}$] (Row 3) and v_r [$\mathrm{km\,s^{-1}}$] (Row 4) at 215 R_S. The white quadrilaterals in Row 2 represent the grid blocks, where the blocks of higher refinement levels are associated with the resulting AMR grid intersected with the solar equatorial plane. In Rows 3 and 4, the black lines denote the magnetic neutral lines.

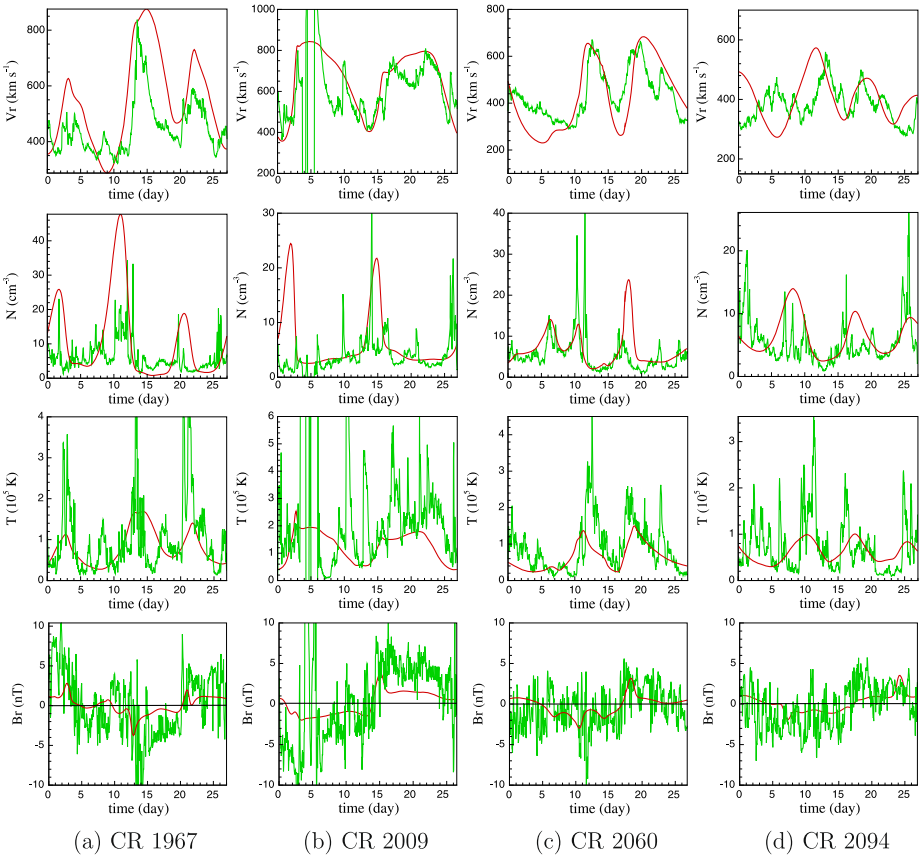

Figure 6 The calculated MHD steady state at 1 AU for CR 1967 (Column a), CR 2009 (Column b), CR 2060 (Column c), and CR 2094 (Column d). The first, second, third, fourth rows are the comparisons between the MHD results and the one-hour averaged OMNI data near 1 AU for radial solar-wind speed $[v_r]$, number density $[N]$, temperature $[T]$, and radial magnetic field $[B_r]$, respectively, where the green lines denote the observations and the red lines represent the numerical results.

at different solar radii and the distribution of solar-wind speed on the solar equatorial plane. The spirals coil more tightly in slow-speed flow than in high-speed flow, as pointed out by Odstrcil and Pizzo (1999). The simulated results on the equatorial planes and at 215 R_s display the structure of corotating interaction regions (CIRs) when the rear ISSs and FSSs overtake the front SSWs, and at 215 R_s the CIRs are evident around $\phi = 160°$ and 340° in CR 2009, $\phi = 140°$ and 200° in CR 2060, and $\phi = 300°$ in CR 2094. It is interesting to notice that for CR 2094 the two-peak and two-valley pattern of the HCS near the Sun become less apparent and more regular near the Earth, due to the interaction between ISWs and SSWs during their outward propagation.

Figure 6 demonstrates the calculated MHD steady solutions at 1 AU for CR 1967 (Column a), CR 2009 (Column b), CR 2060 (Column c), and CR 2094 (Column d). The rows from top to bottom show the comparisons between the MHD results and the one-hour averaged OMNI data near the Earth for radial solar-wind speed $[v_r]$, number density $[N]$, temperature $[T]$, and radial magnetic field $[B_r]$, respectively. Roughly speaking, the steady solutions from our model in Figure 6 can capture the observed changing trends of the solar-

wind parameters in CR 1967, but all three peaks of solar-wind speed decline more slowly than that observed, and have a bit higher speeds and proton number densities. For CR 2009, the model shows two humps in the speed profile, which agrees well with the *in-situ* measurements. However, it should be noted that the first simulated hump rises 1.5 days earlier. The simulation shows the best consistency with the measurements during CR 2060. The simulated maxima in the profiles of v_r, N, and T and their arrivals match the observations reasonably well. The simulation gives a fairly good match in CR 2094 for the two intermediate-speed flows observed from Day 12 to 15 and from Day 17 to 20, but the first one arrives 2.5 days earlier. The relatively large discrepancy between the simulation and the measurements during the first five and the last two days in CR 2094 should come from the significant differences of the photospheric magnetic fields between the start and the end of the CR. Generally speaking, the accuracy of our simulated solar-wind speeds is at the same level as that for other models (*e.g.* Cohen *et al.*, 2008; van der Holst *et al.*, 2010; Riley *et al.*, 2011). From the plots of the radial magnetic field during the four CRs, we can see that the IMF polarities and their changes are captured by our simulations with fairly good accuracy. However, the simulated magnitudes are only one-third to one-half of those from OMNI data for all four CRs, which exist in almost all 3D MHD models of steady and transient solar winds by using the potential field as the initial state (*e.g.* Cohen *et al.*, 2008; van der Holst *et al.*, 2010; Riley *et al.*, 2011; Lugaz *et al.*, 2011).

From the above comparisons, we can see that the simulated results both near the Sun and in interplanetary space reproduce the observations much better for the solar minimum and declining phases than those for the solar maximum and rising phases, which may result from the fact the photospheric magnetic fields around the solar maximum and the rising phase change so rapidly due to their evolution that the changes will cause considerable error if we assume that they basically change little during a CR. Incorporating the daily updated solar magnetograms into the present model may partially improve the situation (Mikić *et al.*, 1999; Arge and Pizzo, 2000). In addition, the discrepancies between the simulations and the observations for the solar maximum and rising phases can partially be attributed to the contaminations by the increasing number of coronal mass ejections.

6. Conclusions and Discussions

In this article, a new SIP–AMR–CESE MHD model is proposed by using our SIP–CESE MHD model on six-component grid with AMR implementation in the context of reference coordinates.

To summarize from the numerical point of view, we have three characteristics:

i) Through the use of the nonsingular transformation introduced here from the physical space to the reference space, the quadrangular frustum pyramid cell for the spherical shell computational domain for solar-wind modeling becomes the conventional rectangular box in the reference space (ξ, η, ζ), which can be seen as the usual Cartesian coordinate. Consequently, the AMR implementation of the code follows easily from PARAMESH in Cartesian coordinate.

ii) More importantly, the transformed governing Equations (4) in the reference space (ξ, η, ζ) for the associated solar-wind plasma flows is still in conserved form. This system can be seen as a PDE in Cartesian coordinates (ξ, η, ζ) on each corresponding component $0 \le \xi \le 14.75$, $\pi/4 - \delta \le \eta \le 3\pi/4 + \delta$, and $3\pi/4 - \delta \le \zeta \le 5\pi/4 + \delta$. Thus, besides the CESE scheme, many other modern numerical schemes in Cartesian coordinates, such as the total variation-diminishing (TVD) scheme and the finite-volume

method (FVM), can be applied directly to the transformed system. This feature provides many flexible alternatives for solving the transformed governing equations in (ξ, η, ζ) and then recover the solution in the physical space through the transformation to obtain the solar-wind solution. That is, many other successful solvers with AMR grids in Cartesian coordinates can be employed as the solar-wind solvers in the context of the present article.

iii) It should be noted that the same CESE solver applies to any coordinate system (such as Cartesian, spherical, cylindrical coordinates, and any other curvilinear coordinates) with only the difference of the coordinate transformation, and consequently the solver proposed here is highly independent of the grid system.

Numerical validations through CRs 1967, 2009, 2060, and 2094 for the solar maximum, declining, minimum, and rising phases are carried out by the newly developed 3D SIP–AMR–CESE MHD model. The numerical simulations have reproduced many features near the Sun during the corresponding solar activity phases. For CR 1967, no PCHs appear at either pole, and only a few ICHs scatter at the low and middle heliographic latitudes. The high-density low-speed regions can be observed everywhere. For CR 2009, LDHS plasma flows from the simulation are coincident with pB measurements from LASCO-C2, and the latitudinal span of the high-density low-speed solar wind is compatible with *Ulysses*' measurements of the solar-wind speed. The numerical results in CR 2060 have some differences from the previous minima demonstrated by other researchers (Tokumaru *et al.*, 2009; Yang *et al.*, 2011). The MNL in CR 2094 displays the structure of two peaks and two valleys, which is also consistent with past results (Hoeksema, Wilcox, and Scherrer, 1983). Many observed interplanetary structures have also been reproduced by the simulations. At 1 AU, the steady solutions from our model have captured the observed changing trends of the solar-wind parameters for all four CRs, except that some peaks of solar-wind speed decline more slowly and arrive no more than three days earlier than observed. In addition, the IMF polarities and their changes are captured by our simulations with fairly good accuracy.

On the one hand, our model can reproduce most of the observed features among the four selected CRs, which are essentially determined by the photospheric magnetic fields, especially their dipole and quadrupole components (Sanderson *et al.*, 2003) and the polar open fields (Wang, Robbrecht, and Sheeley, 2009); on the other hand, we should also note that there exist some differences between the numerical results and observations, such as the magnitude of radial magnetic fields and arrival times of ISWs at the Earth.

Differences occur due to many factors such as the following.

i) The challenging problem of coronal heating and solar-wind acceleration is far from being realistically solved by the specified volumetric heating source term although the topological effect of magnetic field with the expansion factor $[f_s]$ and the angular distance $[\theta_b]$ is considered and, to some extent, can effectively distinguish the high-speed solar wind from the low. 3D two-fluid MHD models, including the effects of different temperatures for protons and electrons in collisionless solar wind (Cranmer *et al.*, 2009; Cranmer, 2010; van der Holst *et al.*, 2010), may improve the simulated plasma parameters of the solar wind. The true physics for the coronal heating/solar-wind acceleration mechanism has to be consolidated as a module in the 3D code in order to better achieve the ambient solar wind. Recently, Wang *et al.* (2011) have shown that incorporating both the line-of-sight magnetic field and transverse velocity into an MHD simulation enables us to obtain bimodal solar wind without any specified the heating function.

ii) The uncertainties of photospheric (especially polar) magnetic measurements and of the potential magnetic field are also important factors leading to the differences between the

observations and numerical results. Although our model is able to reproduce the locations of the coronal-hole boundaries in EIT measurements, the magnitude of open flux tends to be low compared with the *in-situ* measurements at 1 AU, and the discrepancy becomes greater around solar maximum when the *in-situ* IMF can be almost twice as strong as in our model. A great deal of research has revealed that a significant portion of the heliospheric open magnetic flux originates from active regions and coronal mass ejections by means of interchange reconnections (Fisk, Schwadron, and Zurbuchen, 1999; Owens and Crooker, 2006; Riley, 2007; Cohen *et al.*, 2008; Yeates *et al.*, 2010a), which cannot be captured by the potential-field approximation. In addition, the occurrence of some coronal mass ejections (CMEs) during the simulated period and the interaction between solar wind and interplanetary discontinuities, which have been neglected in our model, may also affect the variation trends of solar-wind parameters.

Due to the above-mentioned considerations, several topics need our future attention.

i) Use a more realistic magnetic-field models' output or continuously updated observed photospheric magnetic field as input to drive the ambient solar wind, such as by using non-potential magnetic field model for the Sun's open magnetic flux (*e.g.* Yeates *et al.*, 2010a), surface flux transport (*e.g.* Baumann, Schmitt, and Schüssler, 2006; Cameron *et al.*, 2010; Yeates *et al.*, 2010b), and the synchronic frame format of the solar photospheric magnetic field (*e.g.* Hayashi, Zhao, and Liu, 2008; Zhao, Hoeksema, and Scherrer, 2010, private communication). The projected normal characteristic boundary conditions for such purpose is being established by us in order to improve the time-varying boundary input.
ii) Try a data-driven solar-eruption study by continuously observed data by following the method proposed by Wu *et al.* (2006) and Wang *et al.* (2011). With the AMR–CESE 3D MHD solver available here, continuously observed 3D magnetic field by SOHO/MDI or SDO/HMI become probable as time-dependent boundary input to drive a solar eruptive event.
iii) Consider developing more comprehensive codes to include the models for the lower solar atmospheric layers with the effects of the solar dynamo (*e.g.* Charbonneau, 2005; Hoeksema, 2009) as well as the interchange reconnection in the MHD governing equations.

Acknowledgements The work is jointly supported by the National Natural Science Foundation of China (41031066, 40921063, 40874091, 40890162, 40904050, 40874077, 41074121, and 41074122), 973 program 2012CB825601 and the Specialized Research Fund for State Key Laboratories. S.T. Wu is supported by AFOSR (grant FA9550-07-1-0468), AURA Sub-Award C10569A of NSO's Cooperative Agreement AST 0132798, and NSF (grant ATM-0754378). The numerical calculation has been completed on our SIGMA Cluster computing system. The PARAMESH software used in this work was developed at the NASA Goddard Space Flight Center and Drexel University under NASA's HPCC and ESTO/CT projects and under grant NNG04GP79G from the NASA/AISR project. Wilcox Solar Observatory data used in this study were obtained via http://wso.stanford.edu. The Wilcox Solar Observatory is currently supported by NASA. SOHO is a project of international cooperation between ESA and NASA. The OMNI data is obtained from the GSFC/SPDF OMNIWeb interface http://omniweb.gsfc.nasa.gov. Special thanks go to our reviewer for the invaluable comments on the improvement of the article.

References

Abramenko, V., Yurchyshyn, V., Linker, J., Mikić, Z., Luhmann, J., Lee, C.O.: 2010, Low-latitude coronal holes at the minimum of the 23rd solar cycle. *Astrophys. J.* **712**, 813.

Arge, C.N., Pizzo, V.J.: 2000, Improvement in the prediction of solar wind conditions using near-real time solar magnetic field updates. *J. Geophys. Res.* **105**, 10465.

Arge, C.N., Odstrcil, D., Pizzo, V.J., Mayer, L.R.: 2003, Improved method for specifying solar wind speed near the Sun. In: Velli, M., Bruno, R., Malara, F., Bucci, B. (eds.) *Solar Wind Ten*, *AIP Conf. Ser.* **679**, 190.

Aschwanden, M.J., Burlaga, L.F., Kaiser, M.L., Ng, C.K., Reames, D.V., Reiner, M.J., Gombosi, T.I., Lugaz, N., Manchester, W., Roussev, I.I., Zurbuchen, T.H., Farrugia, C.J., Galvin, A.B., Lee, M.A., Linker, J.A., Mikić, Z., Riley, P., Alexander, D., Sandman, A.W., Cook, J.W., Howard, R.A., Odstrčil, D., Pizzo, V.J., Kóta, J., Liewer, P.C., Luhmann, J.G., Inhester, B., Schwenn, R.W., Solanki, S.K., Vasyliunas, V.M., Wiegelmann, T., Blush, L., Bochsler, P., Cairns, I.H., Robinson, P.A., Bothmer, V., Kecskemety, K., Llebaria, A., Maksimovic, M., Scholer, M., Wimmer-Schweingruber, R.F.: 2008, Theoretical modeling for the STEREO mission. *Space Sci. Rev.* **136**, 565.

Baumann, I., Schmitt, D., Schüssler, M.: 2006, A necessary extension of the surface flux transport model. *Astron. Astrophys.* **446**, 307.

Bilenko, I.A.: 2002, Coronal holes and the solar polar field reversal. *Astron. Astrophys.* **396**, 657.

Bridges, T.J.: 2008, Conservation laws in curvilinear coordinates: A short proof of Vinokur's theorem using differential forms. *Appl. Math. Comput.* **202**, 882.

Cameron, R.H., Jiang, J., Schmitt, D., Schüssler, M.: 2010, Surface flux transport modeling for solar cycles 15-21: Effects of cycle-dependent tilt angles of sunspot groups. *Astrophys. J.* **719**, 264.

Charbonneau, P.: 2005, Dynamo models of the solar cycle. *Living Rev. Solar Phys.* **2**, 2. http://solarphysics.livingreviews.org/Articles/lrsp-2010-3/.

Cohen, O., Sokolov, I.V., Roussev, I.I., Gombosi, T.I.: 2008, Validation of a synoptic solar wind model. *J. Geophys. Res.* **113**, A03104.

Colella, P., Graves, D.T., Keen, N.D., Ligocki, T.J., Martin, D.F., McCorquodale, P.W., Modiano, D., Schwartz, P.O., Sternberg, T.D., Van Straalen, B.: 2007, Chombo software package for AMR applications design document. Technical report, Applied Numerical Algorithms Group, NERSC Division, Lawrence Berkeley National Laboratory Berkeley.

Cranmer, S.R.: 2010, An efficient approximation of the coronal heating rate for use in global Sun-heliosphere simulations. *Astrophys. J.* **710**, 676.

Cranmer, S.R., Matthaeus, W.H., Breech, B.A., Kasper, J.C.: 2009, Empirical constraints on proton and electron heating in the fast solar wind. *Astrophys. J.* **702**, 1604.

De Zeeuw, D.L.: 1993, A quadtree-based adaptively refined Cartesian-grid algorithm for solution of the Euler equations. PhD thesis, Ann Arbor, MI, USA. UMI Order No. GAX94-09674.

Dryer, M.: 2007, Space weather simulation in 3D MHD from the Sun to the Earth and beyond to 100 AU: A modeler's perspective of the present state of the art. *Asian J. Phys.* **16**, 97.

Feng, X., Zhou, Y., Wu, S.T.: 2007, A novel numerical implementation for solar wind modeling by the modified conservation element/solution element method. *Astrophys. J.* **655**, 1110.

Feng, X.S., Xiang, C.Q., Zhong, D.K.: 2011, The state-of-art of three-dimensional numerical study for corona-interplanetary process of solar storms. *Sci. Sin.-Terr.* **41**, 1 (in Chinese).

Feng, X., Yang, L., Xiang, C., Wu, S.T., Zhou, Y., Zhong, D.: 2010, Three-dimensional solar wind modeling from the Sun to Earth by a SIP–CESE MHD model with a six-component grid. *Astrophys. J.* **723**, 300.

Feng, X., Zhang, S., Xiang, C., Yang, L., Jiang, C., Wu, S.T.: 2011, A hybrid solar wind model of the CESE+HLL method with a Yin-Yang overset grid and an AMR grid. *Astrophys. J.* **734**, 50.

Fisk, L.A., Schwadron, N.A., Zurbuchen, T.H.: 1999, Acceleration of the fast solar wind by the emergence of new magnetic flux. *J. Geophys. Res.* **104**, 19765.

Fryxell, B., Olson, K., Ricker, P., Timmes, F.X., Zingale, M., Lamb, D.Q., MacNeice, P., Rosner, R., Truran, J.W., Tufo, H.: 2000, FLASH: An adaptive mesh hydrodynamics code for modeling astrophysical thermonuclear flashes. *Astrophys. J. Suppl. Ser.* **131**, 273.

Garaizar, X., Hornung, R., Kohn, S.: 1999, Structured adaptive mesh refinement applications infracture. Technical report, Lawrence Livermore National Laboratory.

Gombosi, T.I., De Zeeuw, D.L., Powell, K.G., Ridley, A.J., Sokolov, I.V., Stout, Q.F., Tóth, G.: 2003, Adaptive mesh refinement for global magnetohydrodynamic simulation. In: Büchner, J., Dum, C., Scholer, M. (eds.) *Space Plasma Simulation*, *Lecture Notes in Physics* **615**, Springer, Berlin, 247.

Harvey, K.L., Recely, F.: 2002, Polar coronal holes during cycles 22 and 23. *Solar Phys.* **211**, 31.

Hayashi, K.: 2005, Magnetohydrodynamic simulations of the solar corona and solar wind using a boundary treatment to limit solar wind mass flux. *Astrophys. J. Suppl. Ser.* **161**, 480.

Hayashi, K., Zhao, X.P., Liu, Y.: 2008, MHD simulations of the global solar corona around the Halloween event in 2003 using the synchronic frame format of the solar photospheric magnetic field. *J. Geophys. Res.* **113**, 7104.

Hoeksema, J.T.: 2009, Evolution of the large-scale magnetic field over three solar cycles. In: Kosovichev, A.G., Andrei, A.H., Roelot, J.P. (eds.) *IAU Symposium* **264**, Cambridge University Press, Cambridge, 222.

Hoeksema, J.T., Wilcox, J.M., Scherrer, P.H.: 1983, The structure of the heliospheric current sheet: 1978–1982. *J. Geophys. Res.* **88**, 9910.

Jiang, C., Feng, X., Zhang, J., Zhong, D.: 2010, AMR simulations of magnetohydrodynamic problems by the CESE method in curvilinear coordinates. *Solar Phys.* **267**, 463.

Linde, T.: 2002, MHD simulations with the FLASH code. *APS Meeting Abstracts*, F3005.

Lionello, R., Linker, J.A., Mikić, Z.: 2009, Multispectral emission of the Sun during the first whole Sun month: Magnetohydrodynamic simulations. *Astrophys. J.* **690**, 902.

Lugaz, N., Downs, C., Shibata, K., Roussev, I.I., Asai, A., Gombosi, T.I.: 2011, Numerical investigation of a coronal mass ejection from an Anemone active region: Reconnection and deflection of the 2005 August 22 eruption. *Astrophys. J.* **738**, 127.

Luhmann, J.G., Lee, C.O., Li, Y., Arge, C.N., Galvin, A.B., Simunac, K., Russell, C.T., Howard, R.A., Petrie, G.: 2009, Solar wind sources in the late declining phase of cycle 23: Effects of the weak solar polar field on high speed streams. *Solar Phys.* **256**, 285.

MacNeice, P., Olson, K.M., Mobarry, C., de Fainchtein, R., Packer, C.: 2000, Paramesh: A parallel adaptive mesh refinement community toolkit. *Comput. Phys. Commun.* **126**, 330.

Marder, B.: 1987, A method for incorporating Gauss' law into electromagnetic PIC codes. *J. Comput. Phys.* **68**, 48.

McComas, D.J., Elliott, H.A., Gosling, J.T., Reisenfeld, D.B., Skoug, R.M., Goldstein, B.E., Neugebauer, M., Balogh, A.: 2002, Ulysses' second fast-latitude scan: Complexity near solar maximum and the reformation of polar coronal holes. *Geophys. Res. Lett.* **29**, 1290.

McComas, D.J., Elliott, H.A., Schwadron, N.A., Gosling, J.T., Skoug, R.M., Goldstein, B.E.: 2003, The three-dimensional solar wind around solar maximum. *Geophys. Res. Lett.* **30**, 1517.

McComas, D.J., Elliott, H.A., Gosling, J.T., Skoug, R.M.: 2006, Ulysses observations of very different heliospheric structure during the declining phase of solar activity cycle 23. *Geophys. Res. Lett.* **33**, 9102.

Mignone, A., Bodo, G., Massaglia, S., Matsakos, T., Tesileanu, O., Zanni, C., Ferrari, A.: 2007, PLUTO: A numerical code for computational astrophysics. *Astrophys. J. Suppl. Ser.* **170**, 228.

Mikić, Z., Linker, J.A., Schnack, D.D., Lionello, R., Tarditi, A.: 1999, Magnetohydrodynamic modeling of the global solar corona. *Phys. Plasmas* **6**, 2217.

Nakamizo, A., Tanaka, T., Kubo, Y., Kamei, S., Shimazu, H., Shinagawa, H.: 2009, Development of the 3-D MHD model of the solar corona–solar wind combining system. *J. Geophys. Res.* **114**, 7109.

Odstrcil, D., Pizzo, V.J.: 1999, Distortion of the interplanetary magnetic field by three-dimensional propagation of coronal mass ejections in a structured solar wind. *J. Geophys. Res.* **104**, 28225.

Olson, K.: 2006, Paramesh: A parallel adaptive grid tool. In: James, M., Gunther, B., Nobuyuki, S., Akin, E., Anil, D. (eds.) *Parallel Computational Fluid Dynamics 2005: Theory and Applications: Proceedings of the Parallel CFD Conference*, Elsevier, Amsterdam, 341.

Owens, M.J., Crooker, N.U.: 2006, Coronal mass ejections and magnetic flux buildup in the heliosphere. *J. Geophys. Res.* **111**, A10104.

Owens, M.J., Spence, H.E., McGregor, S., Hughes, W.J., Quinn, J.M., Arge, C.N., Riley, P., Linker, J., Odstrcil, D.: 2008, Metrics for solar wind prediction models: Comparison of empirical, hybrid, and physics-based schemes with 8 years of l1 observations. *Space Weather* **6**, S08001.

Parashar, M.: 2007, Grace grid adaptive computational engine. Technical report, Rutgers University.

Pätzold, M., Tsurutani, B.T., Bird, M.K.: 1997, An estimate of large-scale solar wind density and velocity profiles in a coronal hole and the coronal streamer belt. *J. Geophys. Res.* **102**, 24151.

Porfir'eva, G.A., Yakunina, G.V., Delone, A.B., Oreshina, A.V., Oreshina, I.V.: 2009, Coronal streamers on the Sun and their physical properties. *J. Phys. Stud.* **13**, 2901.

Powell, K.G., Roe, P.L., Linde, T.J., Gombosi, T.I., de Zeeuw, D.L.: 1999, A solution-adaptive upwind scheme for ideal magnetohydrodynamics. *J. Comput. Phys.* **154**, 284.

Rendleman, C.A., Beckner, V.E., Lijewski, M., Crutchfield, W., Bell, J.B.: 2000, Parallelization of structured, hierarchical adaptive mesh refinement algorithms. *Comput. Vis. Sci.* **3**, 147.

Riley, P.: 2007, An alternative interpretation of the relationship between the inferred open solar flux and the interplanetary magnetic field. *Astrophys. J. Lett.* **667**, L97.

Riley, P., Linker, J.A., Mikić, Z., Lionello, R., Ledvina, S.A., Luhmann, J.G.: 2006, A comparison between global solar magnetohydrodynamic and potential field source surface model results. *Astrophys. J.* **653**, 1510.

Riley, P., Lionello, R., Linker, J.A., Mikic, Z., Luhmann, J., Wijaya, J.: 2011, Global MHD modeling of the solar corona and inner heliosphere for the whole heliosphere interval. *Solar Phys.* **274**, 361.

Roussev, I.I., Gombosi, T.I., Sokolov, I.V., Velli, M., Manchester, W. IV, De Zeeuw, D.L., Liewer, P., Tóth, G., Luhmann, J.: 2003, A three-dimensional model of the solar wind incorporating solar magnetogram observations. *Astrophys. J. Lett.* **595**, L57.

Sanderson, T.R., Appourchaux, T., Hoeksema, J.T., Harvey, K.L.: 2003, Observations of the Sun's magnetic field during the recent solar maximum. *J. Geophys. Res.* **108**, 1035.

Smith, E.J.: 2011, Solar cycle evolution of the heliospheric magnetic field: The Ulysses legacy. *J. Atmos. Solar-Terr. Phys.* **73**, 277.

Smith, E.J., Marsden, R.G., Balogh, A., Gloeckler, G., Geiss, J., McComas, D.J., McKibben, R.B., MacDowall, R.J., Lanzerotti, L.J., Krupp, N., Krueger, H., Landgraf, M.: 2003, The Sun and heliosphere at solar maximum. *Science* **302**, 1165.

Stone, J.M., Gardiner, T.A., Teuben, P., Hawley, J.F., Simon, J.B.: 2008, Athena: A new code for astrophysical MHD. *Astrophys. J. Suppl. Ser.* **178**, 137.

Taktakishvili, A., Pulkkinen, A., MacNeice, P., Kuznetsova, M., Hesse, M., Odstrcil, D.: 2011, Modeling of coronal mass ejections that caused particularly large geomagnetic storms using ENLIL heliosphere cone model. *Space Weather* **90**, 6002.

Tanaka, T.: 1994, Finite volume tvd scheme on an unstructured grid system for three-dimensional mhd simulation of inhomogeneous systems including strong background potential fields. *J. Comput. Phys.* **111**, 381.

Tokumaru, M., Kojima, M., Fujiki, K., Hayashi, K.: 2009, Non-dipolar solar wind structure observed in the cycle 23/24 minimum. *Geophys. Res. Lett.* **36**, 9101.

Tóth, G., Sokolov, I.V., Gombosi, T.I., Chesney, D.R., Clauer, C.R., De Zeeuw, D.L., Hansen, K.C., Kane, K.J., Manchester, W.B., Oehmke, R.C., Powell, K.G., Ridley, A.J., Roussev, I.I., Stout, Q.F., Volberg, O., Wolf, R.A., Sazykin, S., Chan, A., Yu, B., Kóta, J.: 2005, Space weather modeling framework: A new tool for the space science community. *J. Geophys. Res.* **110**, 12226.

Tóth, G., van der Holst, B., Sokolov, I.V., De Zeeuw, D.L., Gombosi, T.I., Fang, F., Manchester, W.B., Meng, X., Najib, D., Powell, K.G., Stout, Q.F., Glocer, A., Ma, Y.-J., Opher, M.: 2012, Adaptive numerical algorithms in space weather modeling. *J. Comput. Phys.* **231**, 870.

Usmanov, A.V.: 1996, A global 3-D MHD solar wind model with Alfvén waves. In: Winterhalter, D., Gosling, J.T., Habbal, S.R., Kurth, W.S., Neugebauer, M. (eds.) *AIP Conf. Ser.* **382**, 141.

Usmanov, A.V., Goldstein, M.L.: 2006, A three-dimensional MHD solar wind model with pickup protons. *J. Geophys. Res.* **111**, A07101.

van der Holst, B., Keppens, R.: 2007, Hybrid block-AMR in Cartesian and curvilinear coordinates: MHD applications. *J. Comput. Phys.* **226**, 925.

van der Holst, B., Manchester, W.B., Frazin, R.A., Vásquez, A.M., Tóth, G., Gombosi, T.I.: 2010, A data-driven, two-temperature solar wind model with Alfvén waves. *Astrophys. J.* **725**, 1373.

Vinokur, M.: 1974, Conservation equations of gasdynamics in curvilinear coordinate systems. *J. Comput. Phys.* **14**, 105.

Waldmeier, M.: 1981, Cyclic variations of the polar coronal hole. *Solar Phys.* **70**, 251.

Wang, Y.M., Sheeley, N.R. Jr.: 1990, Solar wind speed and coronal flux-tube expansion. *Astrophys. J.* **355**, 726.

Wang, Y.M., Robbrecht, E., Sheeley, N.R. Jr.: 2009, On the weakening of the polar magnetic fields during solar cycle 23. *Astrophys. J.* **707**, 1372.

Wang, Y.M., Sheeley, N.R. Jr., Walters, J.H., Brueckner, G.E., Howard, R.A., Michels, D.J., Lamy, P.L., Schwenn, R., Simnett, G.M.: 1998, Origin of streamer material in the outer corona. *Astrophys. J. Lett.* **498**, L165. doi:10.1086/311321.

Wang, A.H., Wu, S.T., Tandberg-Hanssen, E., Hill, F.: 2011, Utilization of multiple measurements for global three-dimensional magnetohydrodynamic simulations. *Astrophys. J.* **732**, 19.

Watermann, J., Wintoft, P., Sanahuja, B., Saiz, E., Poedts, S., Palmroth, M., Milillo, A., Metallinou, F.-A., Jacobs, C., Ganushkina, N.Y., Daglis, I.A., Cid, C., Cerrato, Y., Balasis, G., Aylward, A.D., Aran, A.: 2009, Models of solar wind structures and their interaction with the Earth's space environment. *Space Sci. Rev.* **147**, 233.

Wei, F., Feng, X., Cai, H., Zhou, Q.: 2003, Global distribution of coronal mass outputs and its relation to solar magnetic field structures. *J. Geophys. Res.* **108**, 1238.

Wu, S.T., Wang, A.H., Liu, Y., Hoeksema, J.T.: 2006, Data-driven magnetohydrodynamic model for active region evolution. *Astrophys. J.* **652**, 800.

Yang, L., Feng, X., Xiang, C., Zhang, S., Wu, S.T.: 2011, Simulation of the unusual solar minimum with 3D SIP–CESE MHD model by comparison with multi-satellite observations. *Solar Phys.* **271**, 91.

Yeates, A.R., Mackay, D.H., van Ballegooijen, A.A., Constable, J.A.: 2010a, A nonpotential model for the Sun's open magnetic flux. *J. Geophys. Res.* **115**, A09112.

Yeates, A.R., Attrill, G.D.R., Nandy, D., Mackay, D.H., Martens, P.C.H., van Ballegooijen, A.A.: 2010b, Comparison of a global magnetic evolution model with observations of coronal mass ejections. *Astrophys. J.* **709**, 1238.

Ziegler, U.: 2008, The NIRVANA code: Parallel computational MHD with adaptive mesh refinement. *Comput. Phys. Commun.* **179**, 227.